NASA/TM-20240012661

Short-Term Elevated Temperature Mechanical Performance and Microstructure of a Niobium-Zirconium Alloy Produced via Laser Powder Bed Fusion In-Situ Alloying

Eric Brizes, Elizabeth Young-Dohe, and Justin Milner
Glenn Research Center, Cleveland, Ohio

October 2024

NASA STI Program Report Series

Since its founding, NASA has been dedicated to the advancement of aeronautics and space science. The NASA scientific and technical information (STI) program plays a key part in helping NASA maintain this important role.

The NASA STI program operates under the auspices of the Agency Chief Information Officer. It collects, organizes, provides for archiving, and disseminates NASA's STI. The NASA STI program provides access to the NTRS Registered and its public interface, the NASA Technical Reports Server, thus providing one of the largest collections of aeronautical and space science STI in the world. Results are published in both non-NASA channels and by NASA in the NASA STI Report Series, which includes the following report types:

- TECHNICAL PUBLICATION.
  Reports of completed research or a major significant phase of research that present the results of NASA programs and include extensive data or theoretical analysis. Includes compilations of significant scientific and technical data and information deemed to be of continuing reference value. NASA counterpart of peer-reviewed formal professional papers but has less stringent limitations on manuscript length and extent of graphic presentations.

- TECHNICAL MEMORANDUM.
  Scientific and technical findings that are preliminary or of specialized interest, e.g., quick release reports, working papers, and bibliographies that contain minimal annotation. Does not contain extensive analysis.

- CONTRACTOR REPORT.
  Scientific and technical findings by NASA-sponsored contractors and grantees.

- CONFERENCE PUBLICATION.
  Collected papers from scientific and technical conferences, symposia, seminars, or other meetings sponsored or cosponsored by NASA.

- SPECIAL PUBLICATION.
  Scientific, technical, or historical information from NASA programs, projects, and missions, often concerned with subjects having substantial public interest.

- TECHNICAL TRANSLATION.
  English-language translations of foreign scientific and technical material pertinent to NASA's mission.

Specialized services also include organizing and publishing research results, distributing specialized research announcements and feeds, providing information desk and personal search support, and enabling data exchange services.

For more information about the NASA STI program, see the following:

- Access the NASA STI program home page at http://www.sti.nasa.gov

NASA/TM-20240012661

Short-Term Elevated Temperature Mechanical Performance and Microstructure of a Niobium-Zirconium Alloy Produced via Laser Powder Bed Fusion In-Situ Alloying

Eric Brizes, Elizabeth Young-Dohe, and Justin Milner
Glenn Research Center, Cleveland, Ohio

National Aeronautics and
Space Administration

Glenn Research Center
Cleveland, Ohio 44135

October 2024

Acknowledgments

Refractory metal research at NASA Glenn Research Center was funded by the Refractory Alloy Additive Manufacturing Build Optimization (RAAMBO) project. This work was made possible through the assistance of multiple staff members in the NASA Glenn Research Center, High Temperature and Smart Alloys branch. We would like to acknowledge the technical inputs from Aaron Thompson, Austin Whitt, Frank Ritzert, Dereck Johnson, Drew Davidson, and Chris Kantzos to the chemical analysis, mechanical testing, preparation of samples, and the electron microscopy conducted.

Level of Review: This material has been technically reviewed by technical management.

This report is available in electronic form at https://www.sti.nasa.gov/ and https://ntrs.nasa.gov/

NASA STI Program/Mail Stop 050
NASA Langley Research Center
Hampton, VA 23681-2199

Short-Term Elevated Temperature Mechanical Performance and Microstructure of a Niobium-Zirconium Alloy Produced via Laser Powder Bed Fusion In-Situ Alloying

Eric Brizes, Elizabeth Young-Dohe, and Justin Milner
National Aeronautics and Space Administration
Glenn Research Center
Cleveland, Ohio 44135

Abstract

Nb-1Zr is a readily fabricable, dispersion-strengthened niobium alloy with improved elevated temperature properties compared to commercially pure niobium. This low to moderate strength niobium alloy is desirable in thermal management systems for fission power and propulsion applications; however, pre-alloyed spherical feedstock for powder-based additive manufacturing processes is generally unavailable. Laser powder bed fusion (L-PBF) in-situ alloying of a Nb-1Zr chemistry was performed using a high-purity niobium feedstock coated with 1 wt% of zirconium-based ceramic compound nano-powders: ZrO_2, ZrC, and ZrH_2. The additively manufactured material was mechanically tested at elevated temperatures within a controlled environment in the as-built condition. For comparison, traditionally manufactured wrought feedstock was also tested within an identical environment. Examination of the materials' microstructure and short-term elevated temperature mechanical response determined: in-situ alloying of spherical Nb powder feedstock with Zr-based ceramic nanoparticles can be successfully implemented; the ZrO_2 addition offered the greatest elevated temperature stability and strength but exhibited brittle behavior; the ZrC addition achieved a balance of room temperature ductility and elevated temperature strength; and the ZrH_2-modified material had the lowest as-built interstitial content and showed high ductility with mechanical performance most similar to wrought Nb-1Zr.

Abbreviations

AM	additive manufacturing
APS	average particle size
EBSD	electron backscatter diffraction
ECD	equivalent circle diameter
EDM	electrical discharge machining
EDS	energy dispersive spectroscopy
GOS	grain orientation spread
IPF	inverse pole figure
L-PBF	laser powder bed fusion
MOS	maximum orientation spread
MUD	multiple of uniform distribution
ODS	oxide dispersion strengthened
SEM	scanning electron microscopy

1.0 Introduction

Niobium (Nb) and its alloys are highly regarded for their exceptional properties in high-temperature applications due to their high melting point (2469 °C), excellent mechanical strength, and creep resistance. However, their inherent properties, particularly strength, can be further enhanced through alloying with specific elements. Nb-Zr alloys exemplify this concept, demonstrating superior strength and creep resistance compared to commercially pure Nb at elevated temperatures. Within the Nb-Zr alloy system, Nb-1Zr and PWC-11 emerge as a particularly promising alloys, offering a unique combination of properties that make them well-suited for use in thermal management systems for aerospace fission power and propulsion applications. Future space power systems require electrical power levels ranging from several hundred kilowatts to many megawatts, exceeding the capability of current photovoltaics or batteries. Dynamic power-conversion systems like Stirling, Brayton, or Rankine cycles show promise for these higher power level systems. In such systems, advanced materials like Nb-1Zr and PWC-11 are crucial to meet the stringent size and performance requirements, with operating temperatures exceeding 1077 °C and lifespans of 7 to 10 years (Ref. 1).

Nb-1Zr [wt%] and PWC-11 (Nb-1Zr-0.1C [wt%]) represent a class of dispersion-strengthened Nb alloys known for their improved elevated temperature properties when compared to commercially pure Nb. The enhancement in mechanical properties in these alloys is attributed to the formation of a dispersion-strengthened microstructure, wherein finely dispersed second-phase particles hinder dislocation movement and grain boundary sliding, thus leading to enhanced strength and creep resistance. Zirconium (Zr) serves as the primary element for forming these second-phase particles, typically in the form of ZrO_2 or (Nb,Zr)C precipitates within the Nb matrix (Ref. 2). However, complications occur as dispersion-forming alloying additions lose their strength advantage at temperatures permitting dislocation climb, and align along grain boundaries contributing to localized high interstitial impurity contents that weaken grain-grain bonds and serve as crack initiation sites (Ref. 3).

In the realm of additive manufacturing (AM), particularly powder-based processes like laser powder bed fusion (L-PBF), the availability of pre-alloyed spherical feedstock for Nb-based alloys such as Nb-1Zr is often limited. This scarcity poses a significant challenge for the fabrication of complex components with desired microstructural features and mechanical properties using AM techniques. To address this challenge, researchers at NASA Glenn Research Center are exploring the concept of in-situ alloying during the L-PBF process to produce Nb-1Zr alloys directly from elemental powders. In this approach, high-purity Nb feedstock is utilized as the base material, onto which a nano-sized Zr-based ceramic compound powder coating is applied. The nano-powders selected for in-situ alloying in this work include ZrO_2, ZrC, and ZrH_2. Each examined ceramic compound has a unique role in facilitating the alloying process and exerts a profound influence on the resulting microstructure and mechanical properties of the final material.

Zirconium oxide, or zirconia (ZrO_2), nanoparticles were chosen for incorporation because they share the same dispersed particle structure within wrought Nb-1Zr and these particles have demonstrated the ability to impede recrystallization and grain growth during exposure to high temperatures (Ref. 4). Within the wrought Nb-1Zr alloy, zirconium reduces the solubility of oxygen in Nb and interacts with oxygen to form ZrO_2, which precipitates into a fine dispersion (Ref. 5). This resulting oxide dispersion strengthening (ODS), effectively inhibits dislocation motion and grain boundary sliding, resulting in superior strength and resistance to creep at elevated temperatures. However, ODS of Nb does not come without restrictions. An excess of oxygen content can lead to increased hardness and brittleness, as well as reduced thermal stability (Ref. 6). The coagulation of oxides in Nb-Zr alloys typically initiates at temperatures between 900 and 1000 °C for exposures lasting 10 hr and at 1200 °C for exposures lasting

30 min (Ref. 4). The extent of hardening during aging diminishes with rising oxygen content, indicating an upper limit of 1.5 to 2 mol% oxide. Peak effectiveness of oxide strengthening is observed when the ZrO_2 content remains below 1 to 1.5 mol% and the operating temperature remains under 1200 °C. It is anticipated the oxide additions would elicit the largest gain in elevated temperature strength because historically, oxide hardening of Nb has proven more potent that carbide or nitride hardening (Ref. 7).

Zirconium carbide (ZrC) nanoparticles were chosen for in-situ alloying due to their exceptional properties, including one of the highest known melting points among binary compounds (~3532 °C), suggesting that the particles may remain solid in superheated Nb melt pools. The expectation is that upon Nb solidification, these solid nanoparticles will serve as heterogeneous nucleation sites, facilitating the precipitation of a fine-grained material when printed via Laser Powder Bed Fusion (L-PBF). Also, in the case of ZrC decomposition, both zirconium and carbon exhibit a strong affinity for interstitials like oxygen, acting as reducing agents. Furthermore, several studies have investigated the impact of carbon content on the microstructure and properties of Nb-Zr alloys. For instance, PWC-11 has demonstrated 3 to 4 times higher short-term tensile creep strength compared to Nb-1Zr, attributed to the presence of fine precipitates of $(Nb,Zr)_2C$ and (Nb,Zr)C. However, the long-term effectiveness of these precipitates remains uncertain (Ref. 1).

Recent research by Vishwandah et al. has provided detailed insights into the Nb-1Zr-0.1C complex carbide formation and aging processes (Refs. 8 and 9). Their work indicates that zirconium tends to preferentially diffuse into the α-Nb_2C carbide phase during extrusion or heat treatment, destabilizing it and leading to the precipitation of a more stable (Nb,Zr)C phase at the expense of Nb_2C carbides. The morphology of the (Nb,Zr)C phase varies depending on thermomechanical processing, exhibiting either spherical or needle morphology with different orientation relationships with respect to the Nb matrix. While carbide strengthening of niobium alloys shows promise for second-phase formation and aging, its effectiveness may be limited at temperatures above 1000 °C. Fine (Nb,Zr)C precipitates have been shown to be highly stable and effective creep strengtheners in the 1080 °C regime and at concentrations between 1 to 2 mol% (Ref. 10). However, coagulation of dispersed carbides occurs rapidly around 1100 °C, leading to reduced strength, particularly at temperatures exceeding 1200 °C, where carbide dispersion strengthening becomes ineffective.

Additionally, oxygen impurity content should be considered in carbide-strengthened Nb alloy design, as Zr tends to bind with oxygen, reducing its availability to form complex carbides. The preference for ZrO_2 formation over carbide formation is expected when oxygen and carbon are both present in solution, based on free energy of formation values and diffusion rates (Ref. 10). Experimental evidence has shown internal oxidation observed in a Nb-1Zr-0.1C alloy transformed the original carbide phase into ZrO_2 platelets, underscoring the significance of considering environmental factors, especially in Additive Manufacturing (AM) processes where there is less control over the build chamber environment and gaseous oxygen readily diffuses into the printed material.

In-situ alloying using Zirconium hydride (ZrH_2) particles was examined because of its unique ability to decompose at high temperatures and subsequently form hydrogen gas and zirconium metal during the L-PBF process to significantly getter oxygen interstitials. ZrH_2, when subjected to elevated temperatures (typically around 400 to 700 °C) in an oxygen-rich environment, undergoes thermal decomposition liberating hydrogen and forming Zr oxide: $2ZrH_2\ (s) + 3O_2\ (g) + \text{Heat} \rightarrow 2ZrO_2\ (s) + 2H_2O\ (g)$. The controlled formation of ZrO_2 aims to produce an additively manufactured Nb-1Zr alloy with low interstitial content for improved room temperature ductility. The use of hydrides for in-situ alloying of refractory metals has been commonplace for decades in powder metallurgy. More recently, hydride in-situ alloying was studied by Hu et al., where TiH_2 and ZrH_2 were added to commercially pure Mo

feedstock, the mixture was ball milled and sintered in a high temperature hydrogen furnace to produce a chemical composition similar to TZM (a dispersion strengthened Mo alloy) (Ref. 11).

Following consolidation, this study delves into the microstructure and short-term elevated temperature mechanical performance of additively manufactured Nb-1Zr materials. The investigation focuses on evaluating the uniaxial tension mechanical response of the as-built L-PBF specimens at both room temperature in air and at elevated temperatures for a short duration of approximately 30 min in a controlled high-vacuum environment. Through a meticulous array of analyses encompassing chemical composition measurements, density measurements, fractography, and detailed metallurgical investigations, this research provides an expansive understanding of how ceramic particle addition influences the microstructure and mechanical performance of high purity Nb. For a comparative analysis, traditionally manufactured wrought barstock of Nb-1Zr also underwent identical microstructural analysis and mechanical testing.

Determination and comparison of the mechanical behavior of the additively manufactured Nb-1Zr materials with that of conventionally manufactured counterparts provides valuable insights into the feasibility and performance of the in-situ alloying approach. Furthermore, a comprehensive examination of the microstructure of the additively manufactured Nb-1Zr materials elucidates the effects of different Zr-compound nano-powder additions on grain texture, secondary phase formation, and other microstructural features. This work aims to identify the Zr-based ceramic nano-powder addition that yields the most favorable microstructure with a balance of elevated temperature strength and room temperature ductility, as well as evaluate the feasibility of the in-situ alloying approaches for fabricating Nb-1Zr alloys.

2.0 Experimental

2.1 Materials and Powder Processing

Conventionally manufactured Nb-1Zr in the wrought condition served as a basis of comparison to the additively manufactured Nb-1Zr in this study. High purity (99.9 percent) Nb spherical powder was used as the primary feedstock for L-PBF. The Nb powder had a particle size distribution of $D_{10} = 21.1$ μm, $D_{90} = 50.4$ μm. Electron images of the Nb powder are shown in Figure 1(a). The Nb powder is a mixture of spherical and nonspherical morphologies. The nonspherical particles have both rounded-with-satellites and angular shapes. The surface of the powder was dotted with nano-sized particles that are likely Nb oxides, but their exact composition was not determined.

The Nb feedstock was modified in batches with 1 wt% additions of either 99.9 percent zirconia (ZrO_2) nanoparticles having an average particle size (APS) of 20 to 40 nm, 99 percent zirconium carbide (ZrC) nanoparticles having an APS of 20 nm, or 99 percent zirconium hydride (ZrH_2) micron-sized particles having an APS of 1 to 5 μm. The nano- and micron-sized particles were integrated into the Nb feedstock using acoustic mixing technology. The rapid acceleration achieved in the acoustic mixers created an adhesion of ZrO_2 nanoparticles that coated the Nb powder. In contrast, the ZrC nanoparticles and ZrH_2 microparticles did not form a consistent layer and adhered to the Nb powder in regions of micron-sized chunks and submicron-sized agglomerates. Electron images of the ZrO_2-, ZrC-, and ZrH_2-modified feedstocks are provided in Figure 1(b) to (d), respectively. Following mixing, the modified batches of spherical Nb were consolidated via L-PBF.

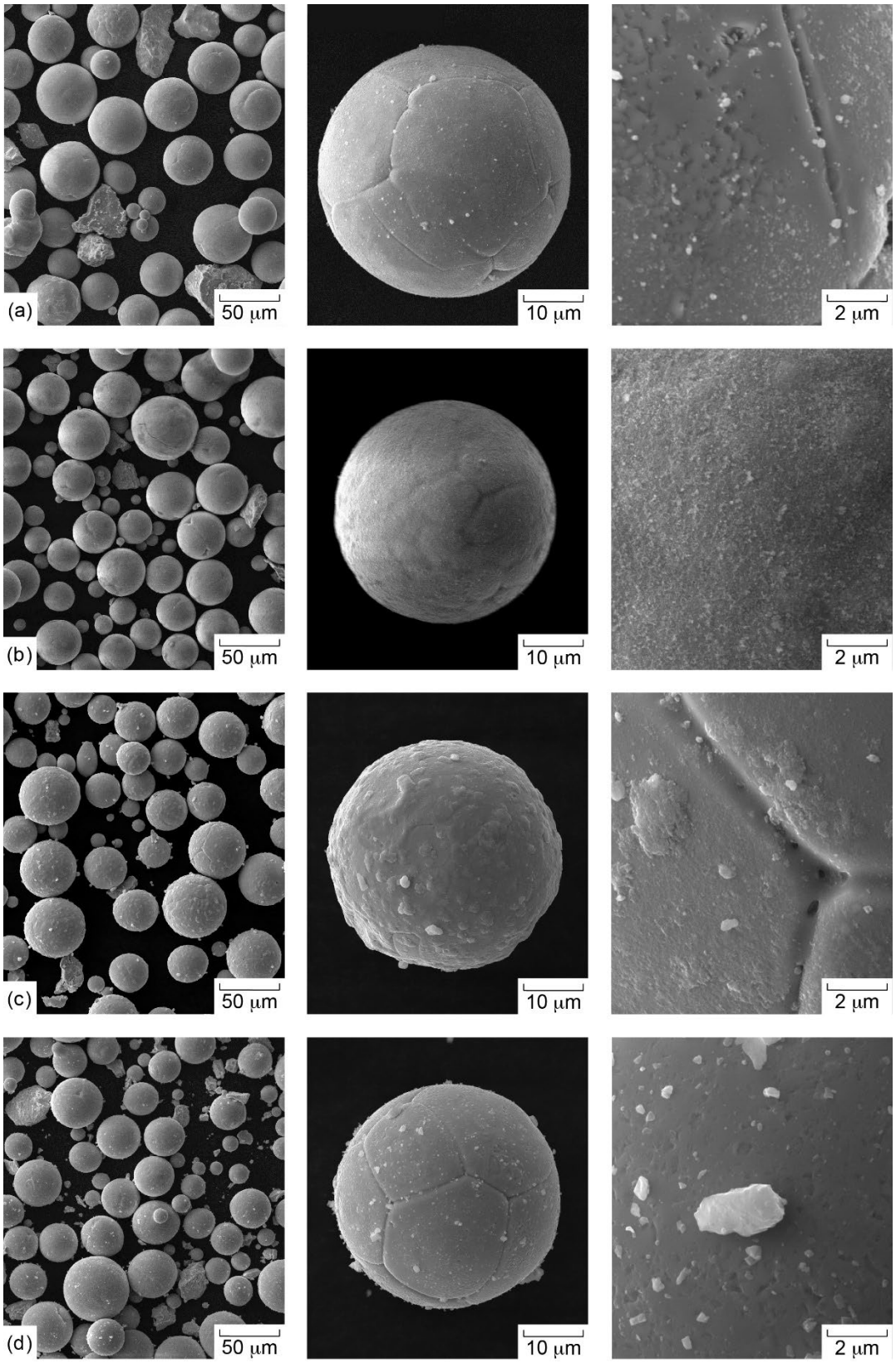

Figure 1.—Powder SEM secondary electron images of (a) pure Nb; (b) Nb + 1 wt% ZrO_2; (c) Nb + 1 wt% ZrC; (d) Nb + 1 wt% ZrH_2.

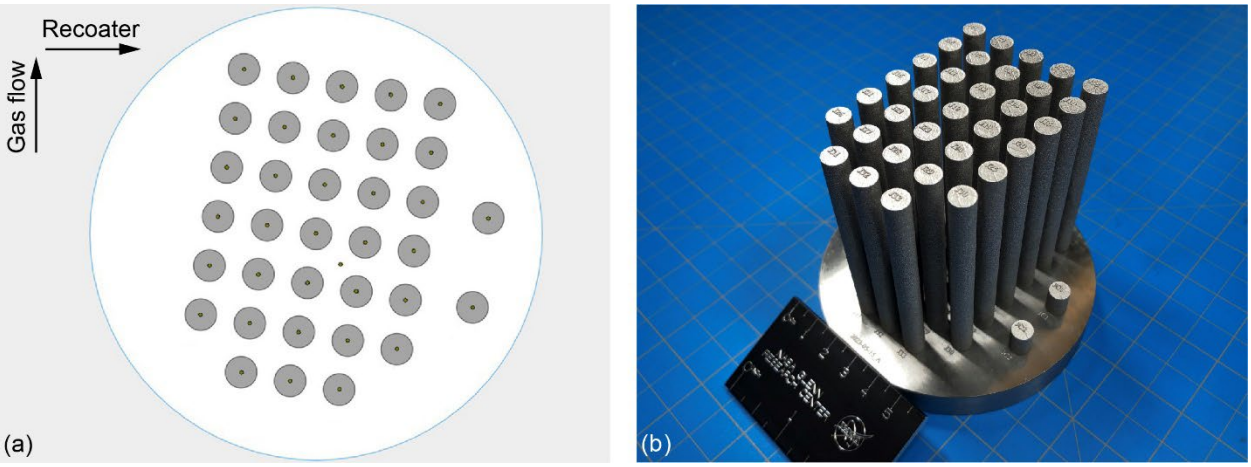

Figure 2.—(a) Layout of specimens on build plate and (b) as-fabricated or as-built specimens.

TABLE 1.—L-PBF PROCESS PARAMETERS

Power, W	Layer thickness, mm	Hatch distance, mm	Scan speed mm/s	Chamber O_2, ppm
170	0.02	0.06	690	<10

2.2 Additive Manufacturing

L-PBF was performed using an *EOS M100* machine which has a 200 W Yb:YAG laser with a wavelength of 1064 nm and a Gaussian spot diameter of 40 μm. An inert argon atmosphere maintained an oxygen content of <10 ppm in the build chamber. The *M100* machine is equipped with a 100-watt heated build plate, but the heating capability was inactive during all printing operations in this study. A total of three prints were performed: Nb + 1 wt% ZrO_2 (Nb-1ZrO_2), Nb + 1 wt% ZrC (Nb-1ZrC), and Nb + 1 wt% ZrH_2 (Nb-1ZrH_2). For each print, thirty-three cylinders with a diameter of 7 mm and height of 70 mm were arranged vertically on the build plate in rows of five, 10° askew of the machine's recoating direction (Figure 2). Two smaller cylinders of the same diameter and 10 mm in height were placed to the side as witness coupons for measurement of material chemical composition and density. Process parameters were determined from an exhaustive optimization study that measured the influence of laser power, laser scan speed, and hatch spacing to maximize material relative density and are provided in Table 1.

2.3 Mechanical Testing

An electrical discharge machining (EDM) cut first removed the cylindrical specimens and witness coupons from the build plate. One cylinder of each material including the wrought Nb-1Zr barstock underwent a hammer-bend screening test to compare room temperature ductility in the as-built/wrought conditions. Cylinders were secured in a vise and struck with a hammer until failure or the completion of a 90-degree bend. Results of the hammer-bend test are shown in Figure 3. Observationally, both the wrought Nb-1Zr and as-built Nb-1ZrH_2 material exhibited sufficient room temperature ductility to achieve a 90° bend. The as-built Nb-1ZrC withstood a few degrees of bending before failing at a single position near the axis of bending. The as-built Nb-1ZrO_2 material shattered immediately in two locations near the axis of bending and at the area of hammer impact.

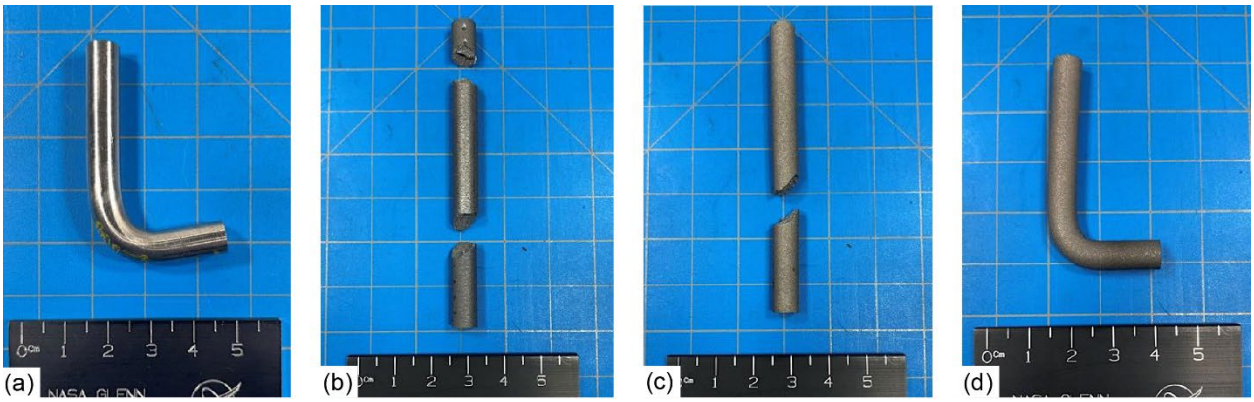

Figure 3.—Hammer-bend test results for wrought and as-built L-PBF consolidated materials. (a) Wrought Nb-1Zr. (b) Nb-1ZrO_2. (c) Nb-1ZrC. (d) Nb-1ZrH_2.

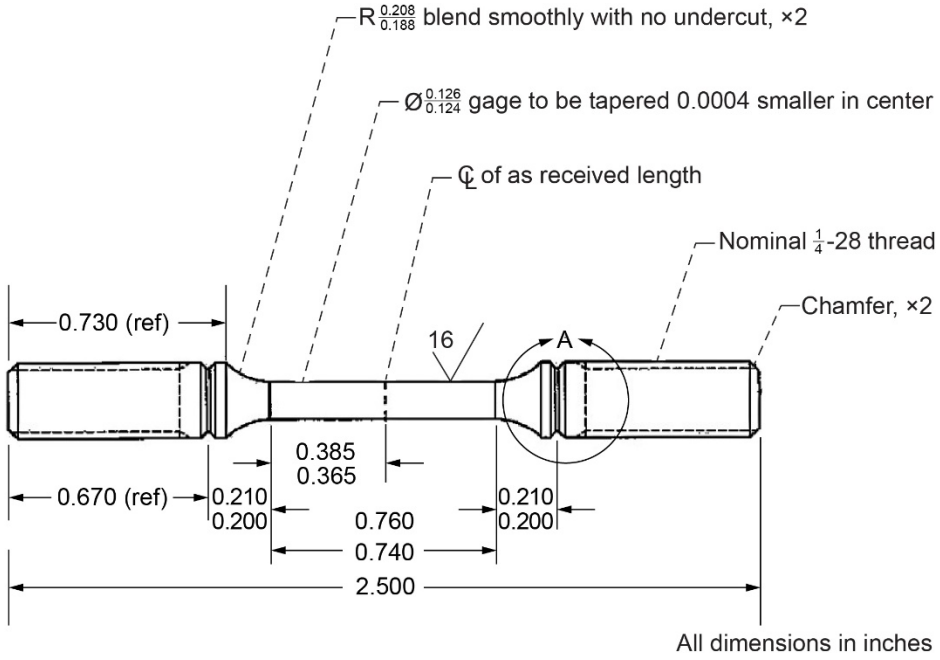

Figure 4.—Uniaxial tension specimen geometry.

Each of the remaining as-built cylinders were then precision machined to the dog-bone geometry shown in Figure 4. The wrought Nb-1Zr specimens were similarly prepared. Uniaxial tension was performed at room temperature in air and at elevated temperature in vacuum. At room temperature, two tests were performed for each material and sample strain was measured using a laser extensometer. Vacuum mechanical testing was conducted using modernized legacy equipment at NASA Glenn Research Center (GRC). A high-vacuum environment is required for elevated temperature testing of refractory alloys to prevent oxidation and interstitial embrittlement. The high-temperature/vacuum load frame is screw-driven, has a tungsten mesh resistive heating element, and employed a diffusion pump to maintain a vacuum level less than 1E-4 Pa for all tests. Only a single test was conducted at an elevated temperature of 1300 °C for each material. Temperature was measured throughout testing using three type-C thermocouples placed along the gauge section of the dog-bone specimens. The entire specimen and thermocouples were wrapped in tantalum foil to prevent oxidation during heat-up. The tensile specimens

experienced the peak temperature during testing for approximately 30 min. A high-temperature extensometer was not used in this work and therefore strain is calculated from crosshead displacement taking equipment compliance into consideration.

2.4 Chemical and Microstructural Analysis

Once the cylindrical witness coupons were removed from their respective build plates, the witness coupons underwent chemical analysis. The materials' chemical compositions measured using inductively coupled plasma mass spectrometry and inert gas fusion are shown in Table 2. Chemical composition was also determined for the wrought Nb-1Zr and the unmodified high-purity Nb powder feedstock.

After elevated temperature mechanical testing, the fracture surfaces of the tension specimens were imaged using a *Tescan MAIA-3* field emission gun scanning electron microscope. The density of each specimen was measured using the Archimedes method with a deionized water submersion fluid. The specimens were then sectioned for electron microscopy. Metallurgical samples from the threaded region of the dog-bone specimens were hot mounted in a conductive thermoset polymer, ground with SiC paper, polished to a 1-μm finish using diamond paste, and vibratory polished with a 50 nm colloidal silica solution. All samples were imaged at a range of magnifications to identify any microstructural differences. During electron imaging, energy dispersive spectroscopy (EDS) and electron backscatter diffraction (EBSD) mapping was conducted on regions of interest. Following electron imaging, optical micrographs were taken to determine relative density using image analysis.

3.0 Results

3.1 Density

The density of metallic materials has a significant impact on mechanical performance and increased relative density correlates to greater strength and improved elastic behavior. Furthermore, minimization of defects within additively manufactured material reduces the number of failure initiation points and easy crack growth paths. The relative density determined via optical microscopy and image analysis of the four examined Nb materials are shown in Figure 5. The wrought Nb-1Zr material was fully dense (>99.99 percent), with limited porosity and no observable cracking. Despite meticulous parameter development for maximized densification, all the as-built L-PBF consolidated materials exhibited porosity defects. The relative densities of the L-PBF materials ranged from 99.69 to 99.89 percent with Nb-1ZrO_2 being least dense (99.69 percent), followed by Nb-1ZrC (99.75 percent), and finally Nb-1ZrH_2 (99.89 percent) achieved the greatest relative density.

TABLE 2.—CHEMICAL COMPOSITION OF THE WROUGHT, Nb POWDER FEEDSTOCK, AND AS-BUILT L-PBF CONSOLIDATED MATERIALS

Material	Nb, wt%	Zr, wt%	O, ppm	N, ppm	C, ppm
Standard ATSM B391 (max.)	Balance	0.8 to 1.2	250	100	100
Wrought	Balance	1.19	250	119	18
Nb powder	Balance	----------	660	120	26
Nb-1ZrO_2	Balance	0.65	2815	232	33
Nb-1ZrC	Balance	0.43	1094	294	576
Nb-1ZrH_2	Balance	0.83	695	278	35

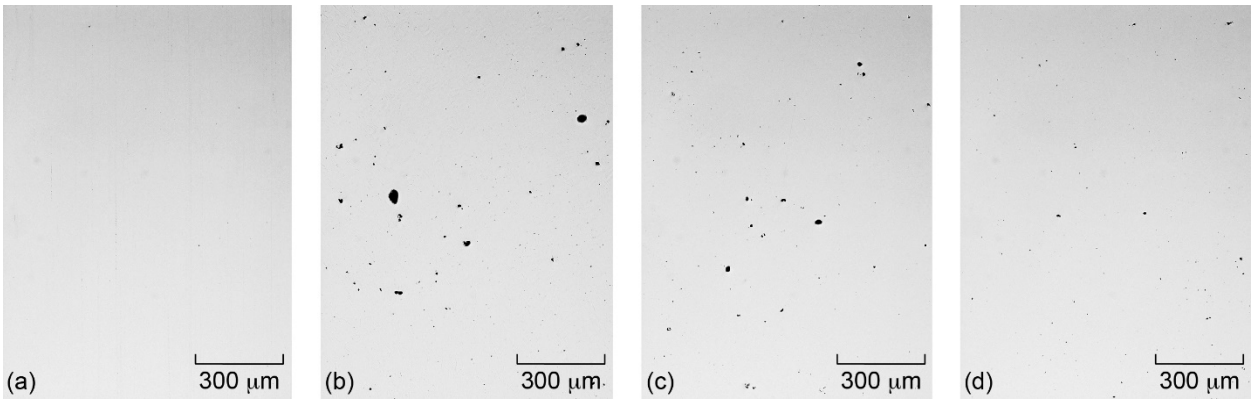

Figure 5.—Examples of optical micrographs from which image analysis determined. (a) Wrought Nb-1Zr. (b) Nb-1ZrO_2. (c) Nb-1ZrC. (d) Nb-1ZrH_2 material relative density.

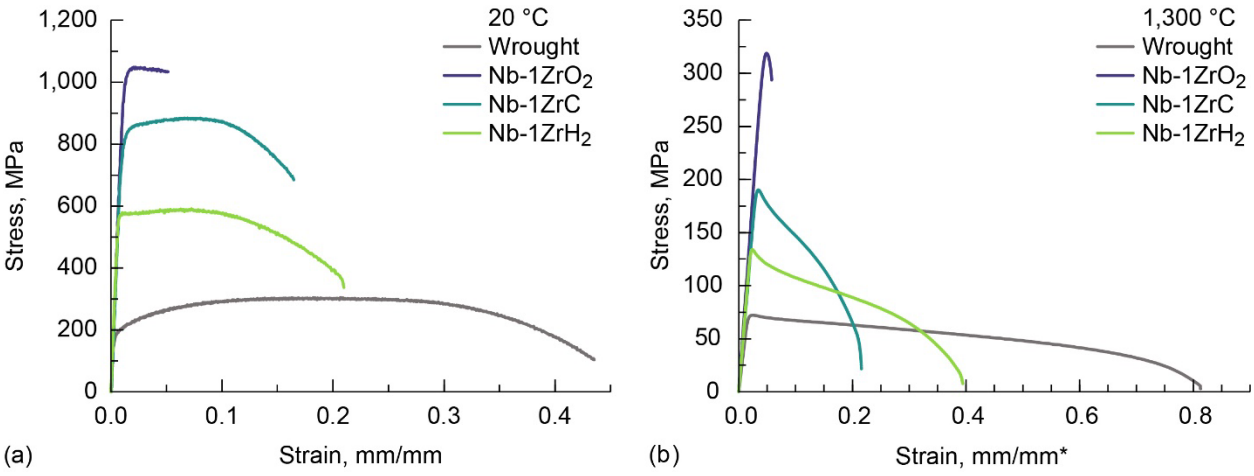

Figure 6.—Room-temperature air. (a) Elevated-temperature high-vacuum. (b) Uniaxial tension testing engineering stress-strain curves for wrought and L-PBF materials. *Estimated as engineering strain was measured using load frame crosshead displacement.

3.2 Room Temperature Air and Elevated Temperature High-Vacuum Tension Testing

The determination of elevated temperature mechanical performance is crucial for refractory metals intended for structural service in such environments. As previously mentioned, high-vacuum is necessary to prevent oxidation and interstitial embrittlement during heat-up and testing. Representative stress vs. strain responses for each of the four studied materials at room and elevated temperature (1300 °C) are presented in Figure 6(a) and (b), respectively. Tabulated uniaxial tension properties are provided in Table 3. Note the room-temperature data represents an average of two tests and the elevated temperature results are a single datum for each material. Reported engineering strain and elastic moduli for the elevated temperature testing are estimates determined from the load frame crosshead displacement.

TABLE 3.—ROOM-TEMPERATURE AND ELEVATED-TEMPERATURE MECHANICAL PROPERTIES OF THE WROUGHT AND L-PBF Nb-1ZR MATERIALS

Material	20 °C				1300 °C			
	EM, GPa	YS, MPa	UTS, MPa	Elongation, percent	EM, GPa[a]	YS, MPa	UTS, MPa	Elongation, percent
Wrought	74.6	184	304	44	20.7	69	72	81
Nb-1ZrO_2	95.1	989	1034	7	34.1	307	319	6
Nb-1ZrC	89.6	802	891	18	30.7	187	190	22
Nb-1ZrH_2	86.8	566	585	20	30.0	133	134	40

[a]Estimated as engineering strain was measured using load frame crosshead displacement.

3.3 Fractography

Low and high magnification secondary electron images of the fracture surfaces for all four examined materials tested at both 20 and 1300 °C are provided in Figure 7. The lower magnification images show the fracture regions outlined in a yellow-dotted line. The higher magnification images exhibit typical surface features for each of the wrought and L-PBF specimens. All materials except the Nb-1ZrO_2 show a significant reduction in area before failure, especially at the elevated 1300 °C temperature. The Nb-1ZrO_2 had brittle cleavage-type fractures on all surfaces. Both the Nb-1ZrC and Nb-1ZrH_2 materials had a mixture of brittle cleavage and ductile dimpling behavior when tested at room-temperature; however, the surface patterns changed significantly indicating increased ductility on the elevated temperature specimens. At 1300 °C, both the wrought Nb-1Zr and Nb-1ZrH_2 L-PBF specimens exhibited tremendous ductility (>40 percent elongation) and that is evident with observable micro-void coalescence within the fracture surfaces.

3.4 Microstructural Analysis

Electron images of the wrought and L-PBF material microstructures at multiple magnifications were taken of both the room and elevated temperature samples and are shown in Figure 8. The images provide qualitative insight into changes in grain size and the formation of precipitate phases once the materials were exposed to elevated temperature (1300 °C for ~30 min). The wrought Nb-1Zr (Figure 8(a)) experienced recrystallization and grain growth as evident by the elimination of the smaller grains that were arranged in the extruded direction of the as-received barstock. The Nb-1ZrO_2 microstructure in Figure 8(b) does not show significant change following the 1300 °C exposure. The Nb-1ZrC and Nb-1ZrH_2 materials in Figure 8(c) and (d), respectively, also show limited evidence of grain growth.

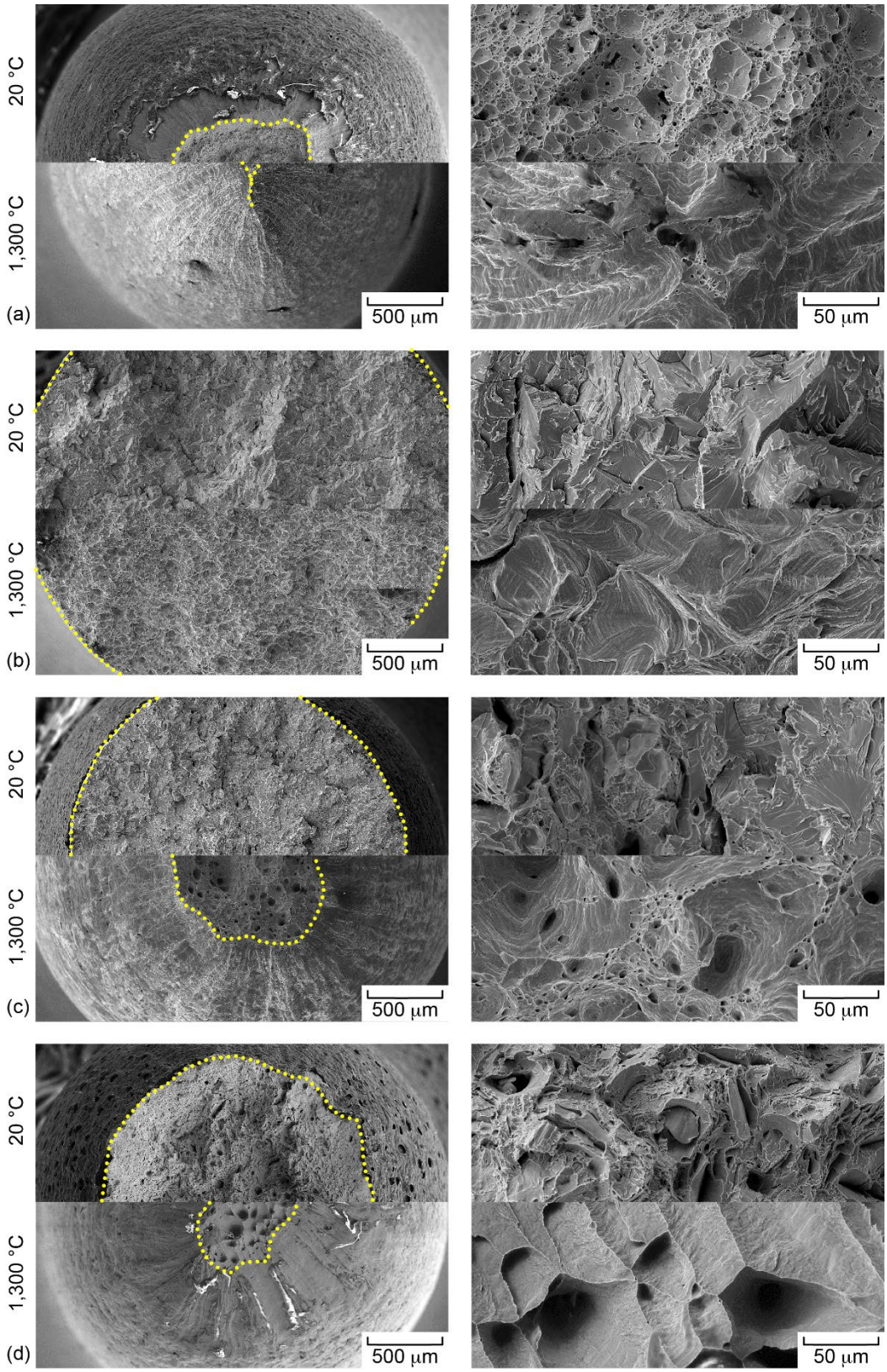

Figure 7.—Low (left, 200x) and high (right, 2,000x) magnification secondary electron images of room-temperature (upper) and elevated temperature (lower). (a) Wrought Nb-1Zr. (b) Nb-1ZrO_2. (c) Nb-1ZrC. (d) Nb-1ZrH_2 fracture surfaces.

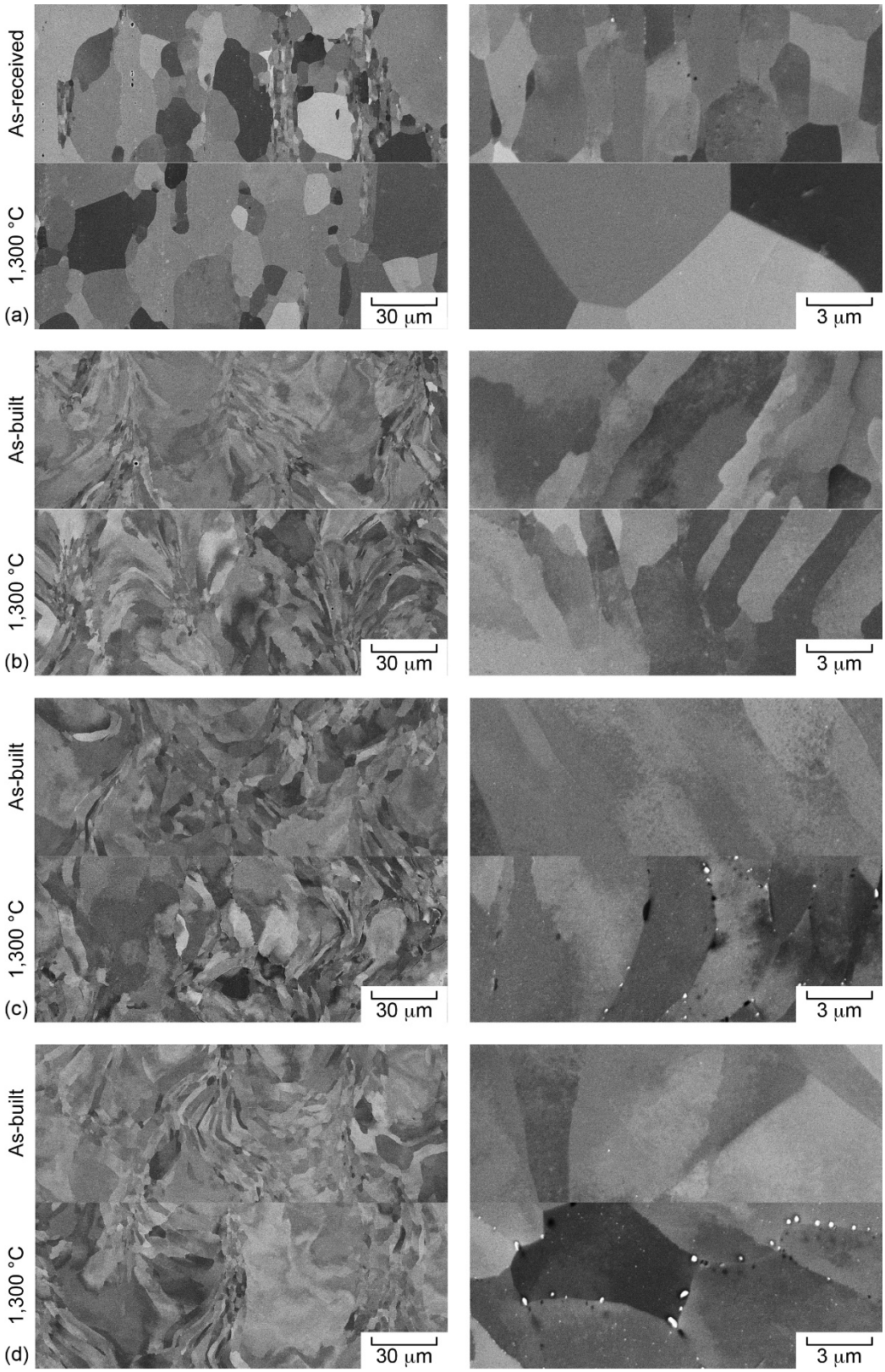

Figure 8.—Low (left, 3,000x) and high (right, 30,000x) magnification secondary electron images. (a) Wrought Nb-1Zr. (b) Nb-1ZrO2. (c) Nb-1ZrC. (d) Nb-1ZrH2 cross-sections in both as-received/built (top) and 1,300 °C exposed (bottom) conditions.

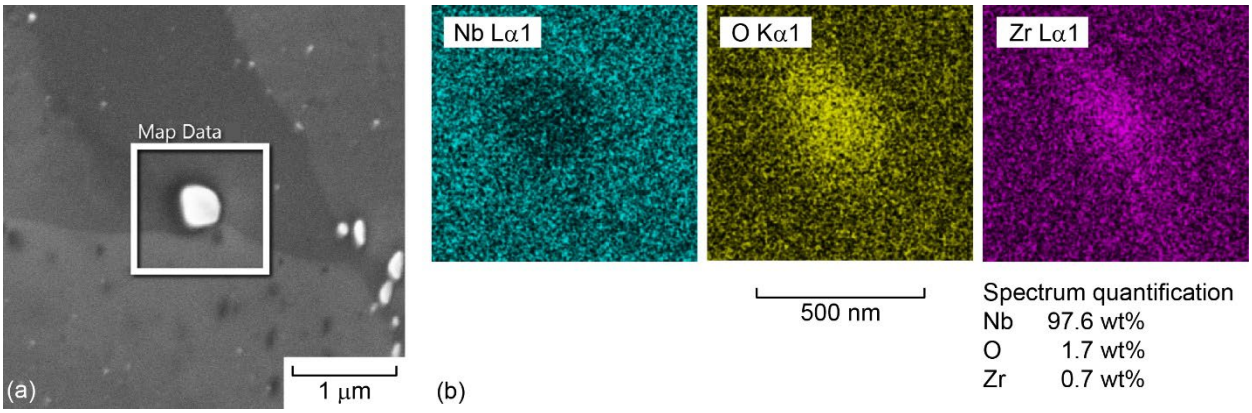

Figure 9.—Secondary electron image and (a) EDS elemental maps (b) of Nb-1ZrH_2 microstructure verifying Zr-rich oxide precipitates at grain boundaries.

However, both experienced precipitate formation and coarsening at the grain boundaries and intragranularly. The precipitates were further examined in both the Nb-1ZrC and Nb-1ZrH_2 materials using EDS. A high magnification electron image alongside EDS element maps are shown in Figure 9. The EDS mapping identified the grain boundary precipitates as a Zr-rich oxide, likely ZrO_2.

EBSD maps and grain statistics quantified the microstructural differences between the wrought and L-PBF consolidated Nb samples, however only the as-built/received microstructures were examined. EBSD mapping was not performed on the materials that experienced the elevated temperature exposure. The grain color map, inverse pole figure (IPF) Z map, and pole figure of the {100} easy growth direction for BCC metals is shown for each of the four studied materials in Figure 10. A detailed report of each material's grain statistics is provided in Table 4. Although unplanned, the wrought and L-PBF materials had similar grain size and grain aspect ratios. All materials had nearly identical textures with the {100} pole figures depicting a MUD ranging from 12.05 to 13.69. The wrought Nb-1Zr and Nb-1ZrO_2 materials had a smaller ECD and lower aspect ratios (6.20/6.00 μm and 2.13/2.15) compared to the Nb-1ZrC and Nb-1ZrH_2 (7.37/7.51 μm and 2.43/2.49). However, out of the printed materials, Nb-1ZrH_2 exhibited GOS and MOS values closest to the wrought Nb-1Zr (1.07/0.97° and 2.49/2.37°).

4.0 Discussion

4.1 Feasibility of L-PBF In-Situ Alloying

To understand the effectiveness of the L-PBF in-situ alloying approach, it is necessary to evaluate the approach's ability to form fully dense microstructures and quantify the yield of the ceramic nanoparticle incorporation into the as-built material needed to reach the 1 wt% Zr target.

The density results in Section 3.1 prove that L-PBF parameter optimization can be implemented to achieve material relative densities of approximately 99.7 percent or greater. A relative density measure of 99.7 percent is typical for metal additive manufacturing and has minimal impact on the printed material's overall mechanical performance (Ref. 12). Furthermore, all defects in the as-built microstructures were porosity or voids which can be closed via post processing steps like hot isostatic pressing. No cracking was observed that would be detrimental to material performance in cyclic loading applications.

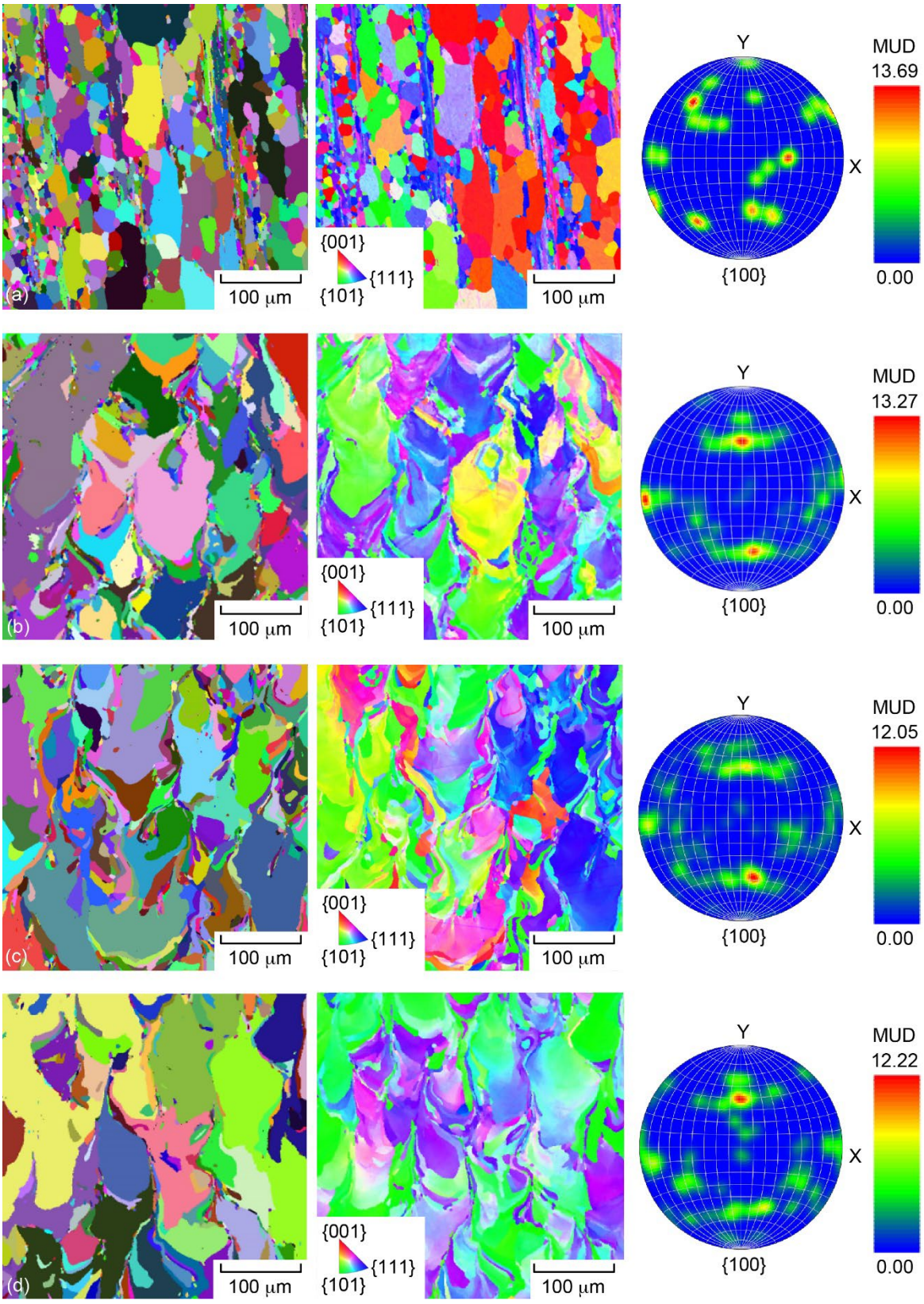

Figure 10.—Grain color maps, EBSD inverse pole figure (IPF) Z maps, and {100} pole figures for (a) wrought Nb-1Zr, (b) Nb-1ZrO_2, (c) Nb-1ZrC, and (d) Nb-1ZrH_2 cross-sections.

TABLE 4.—AVERAGE EBSD GRAIN STATISTICS FOR THE WROUGHT AND L-PBF CONSOLIDATED Nb MATERIALS

Material	EBSD grain statistics (average)				
	ECD, μm	Length, μm	Aspect ratio	GOS, °	MOS, °
Wrought Nb-1Zr	6.20	10.62	2.13	0.97	2.37
Nb-1ZrO_2	6.00	11.18	2.15	1.27	2.82
Nb-1ZrC	7.37	14.43	2.43	1.20	2.93
Nb-1ZrH_2	7.51	15.00	2.49	1.07	2.49

TABLE 5.—DETERMINATIONS OF L-PBF Zr YIELD AND UNREACTED Zr/O FOR THE WROUGHT AND PRINTED Nb-1Zr MATERIALS

Material	L-PBF Zr yield determination			Unreacted Zr/O determination				
	Added Zr, wt%	As-built Zr, wt%	Zr yield, percent	Zr, at.%	O, at.%	Reacted Zr (+O_2), at.%	Unreacted Zr, at.%	Unreacted O, at.%
Wrought	-----	-----	-----	1.21	0.17	0.09	1.13	-----
Nb-1ZrO_2	0.74	0.65	88	0.65	1.60	0.65	-----	0.30
Nb-1ZrC	0.88	0.43	49	0.43	0.63	0.32	0.12	-----
Nb-1ZrH_2	0.98	0.83	85	0.84	0.41	0.21	0.64	-----

The yield of Zr ceramic particle incorporation into the as-built material was determined by comparing the Zr content of the 1 wt% ceramic addition to the Zr content of the as-built printed material (Table 5). The consolidated Nb-1ZrO_2 material contained a Zr content of 0.65 wt% compared to the nanoparticle addition to the Nb feedstock which had a Zr content of 0.74 wt%, indicating a loss of approximately 0.09 wt% Zr during processing or a Zr yield of 88 percent. Mixing and consolidation of the ZrC-modified feedstock experienced the lowest yield of Zr (49 percent) as indicated by the measured 0.43 wt% of Zr relative to the 0.88 wt% Zr added using ZrC nanoparticles to the pure Nb spherical powder. To produce an alloy with a PWC-11 chemical composition, an increased content of 2 wt% ZrC should be mixed within the modified feedstock to account for Zr and C losses. Notably, the ZrH_2 addition was the only in-situ alloying approach that achieved an as-built Zr concentration that met the standard for wrought Nb-1Zr (within 0.8 to 1.2 wt% Zr) (Ref. 13). This is because the 85 percent yield with respect to the 0.98 wt% addition allowed the as-built Zr content to measure 0.83 wt%.

Another aspect to consider for in-situ alloying feasibility is room temperature ductility. A metric often employed during L-PBF design necessitates materials to have a room temperature elongation at failure greater than 10 percent to reduce cracking and accommodate residual stresses that occur during printing of complex geometries. Total elongation measured from the room temperature tensile testing (Table 3) showed that both the Nb-1ZrC and Nb-1ZrH_2 materials exhibited acceptable values of 18 and 20 percent, respectively. It is anticipated that both these materials should be able to print complex parts without cracking. Furthermore, the hammer-bend screening test (Figure 3) effectively demonstrated the superior room temperature ductility of the Nb-1ZrH_2 material. The ZrH_2 incorporation resulted in the lowest as-built oxygen content of 695 ppm (Table 2) amongst the L-PBF consolidated materials. This reduction in oxygen, coupled with the standard (>0.8 wt%) Zr content, is well documented to contribute to the preservation of room temperature ductility in Nb-Zr alloys (Refs. 2, 5, 3, and 14). The limited hammer-

bend ductility of the Nb-1ZrC material may be due to strain rate sensitive mechanical performance characteristics and warrants further investigation.

Adequate room temperature ductility is crucial not only for flawless printing of intricate geometries but also for facilitating subsequent welding processes critical for applications like NASA's meter-long Nb-1Zr heat pipes. Planned heat pipe components require fabrication in sections and employ joining via high-energy-density welding techniques such as electron beam or laser welding. Therefore, sufficient material ductility is paramount to accommodate the thermal strains encountered during welding and ensure the structural integrity of the final component (Ref. 15).

4.2 Influence of the Ceramic Nanoparticle Addition on Microstructure and Chemistry

As conventionally produced Nb-1Zr and PWC-11 are strengthened via a dispersion of ZrO_2 (and (Nb,Zr)C for PWC-11), the as-built L-PBF microstructures also aim to achieve a fine dispersion of oxides and/or carbides. However, verification of oxide/carbide dispersion quality is best performed using advanced transmission electron microscopy (TEM) techniques which were outside the scope of this work. Nevertheless, SEM including EDS and EBSD were able to characterize the microstructure of the as-built and elevated temperature (1300 °C) exposed specimens. The electron microscopy analysis focused on the determination of as-built grain size and texture, as well as the thermal stability of the microstructure via identification of precipitates formed at 1300 °C.

Both the Nb-1ZrC and Nb-1ZrH_2 materials showed the formation of Zr-rich oxide precipitates at grain boundaries and within the grains (intragranular) during high-temperature exposure (Figure 8(c) and (d)). This phenomenon is well documented in Nb-Zr alloys, with studies demonstrating that such grain boundary oxides are detrimental to strength due to the weakening of grain-to-grain adhesion (Refs. 3, 16, 4, and 17). In the Nb-1ZrC material, zirconium-rich carbides or other carbide phases were not directly observed during electron microscopy. But the presence of carbon, as measured via LECO combustion analysis (Table 2), is likely contributing to the strengthening of the material. Regardless, the appearance of these grain boundary precipitates proves that the as-built Nb-1ZrC and Nb-1ZrH_2 microstructures are not stable at 1300 °C.

Conversely, the Nb-1ZrO_2 microstructure showed minimal ZrO_2 formation at grain boundaries (Figure 8(b)) suggesting microstructural thermal stability at 1300 °C. This is attributed to the initial incorporation of Zr already in a nano-sized oxide form, likely as a fine dispersion of ZrO_2. Consequently, the absence of "free" or unreacted Zr (or Zr atoms occupying a substitutional role within the BCC matrix) available to migrate and coarsen into larger precipitates at grain boundaries is believed to be a contributing factor to the exceptional high-temperature strength observed in the Nb-1ZrO_2 alloy. This aligns with the established understanding of the role of metal:oxygen stoichiometry within dispersed oxide strengthening of refractory alloys (Refs. 4 and 7).

The theoretical amount of unreacted (substitutional) Zr in each of the L-PBF printed and wrought materials is provided in Table 5. The amount of unreacted Zr was determined using the Zr and oxygen (O) contents measured by ICP-MS and LECO combustion. All oxygen in the material is assumed to react with Zr to form ZrO_2 in the stoichiometric 1:2 Zr:O atomic ratio. All leftover Zr is labeled unreacted. Or in the context of the Nb-1ZrO_2 material, all leftover oxygen is expected to occupy interstitial sites within the Nb matrix. From this estimate, the wrought Nb-1Zr has 1.13 at% of unreacted Zr, the Nb-1ZrH_2 material has 0.64 at% of unreacted Zr, Nb-1ZrC has 0.12 at% of unreacted Zr, and Nb-1ZrO_2 has an excess oxygen of 0.30 at%. Note the formation of $(Nb,Zr)_2C$ or (Nb,Zr)C is not considered in this estimate. The impact of Zr and O content/ratio on mechanical performance is discussed later in Section 4.3.

Microstructurally, while it is generally accepted that smaller grain size enhances mechanical performance in many metallic materials, this observation is not universally applicable to all alloy systems. And in the case of body-centered cubic (BCC) refractory alloys like those in the Nb-Zr system, testing has shown that reductions in grain size have a limited impact on strength (Ref. 3). This is corroborated in the current study, where EBSD analysis revealed the differences in grain size and texture provided little contribution to the contrasting mechanical behavior between the L-PBF consolidated Nb-1Zr alloys. However, the EBSD-derived GOS and MOS parameters do offer some insights. The Nb-1ZrH_2 material displayed a comparably lower misorientation within grains (2.49 °MOS), similar to the values observed in the reference wrought Nb-1Zr material (2.37 °MOS). This suggests a lower intragranular misorientation microstructure with slip planes that are more likely to completely traverse grains created a lower activation stress to induce strain in Nb-1ZrH_2 compared to the Nb-1ZrO_2 and Nb-1ZrC microstructures, which exhibited marginally smaller grain sizes and a higher degree of misorientation within grains. This increase in misorientation may be related to the specific interaction between ZrO_2 and (Nb,Zr)C nanoparticles and the Nb matrix upon solidification and subsequent processing, requiring further investigation.

4.3 Evaluation of Elevated Temperature Mechanical Performance

Retention of strength at elevated temperatures is a particularly challenging metallurgical problem for Nb-based alloys. Dispersion strengthening is the most effective mechanism for temperatures nearing and exceeding 60 percent of the metal's solidus. As discussed, previous studies of dispersion strengthening of Nb have shown that oxides, carbides, and nitrides based on zirconium or hafnium can strengthen a Nb matrix up to 1200 °C (Ref. 4). Following long-term exposure to temperatures greater than 1200 °C, oxides and carbides tend to coarsen and migrate to grain boundaries leading to a reduced strength and brittle behavior. On this basis, the elevated temperature tensile specimens in this study that experienced a short-term, 30-min exposure at a maximum temperature of 1300 °C may not be able to maintain their respective yield properties long-term. Nevertheless, the elevated temperature mechanical performance of the L-PBF printed materials are analyzed with respect to their chemistry and microstructure.

The addition of 1 wt% ZrO_2 nano-powder significantly enhanced the Nb-1ZrO_2 material's high-temperature mechanical performance. The Nb-1ZrO_2 material achieved a remarkable yield strength of 307 MPa at 1300 °C, exceeding most previously reported values for Nb-based alloys. The yield strength at 1300 °C as a function of density for the materials in this study alongside historical Nb-based alloys like C-103, Cb-752, FS-85, and WC-3015 are shown in Figure 11(d) (Refs. 16, 18, and 19). However, the low ductility (<7 percent elongation at failure) at both room and elevated temperatures is anticipated to limit the alloy's usefulness in aerospace applications, where adequate formability is often crucial. The Nb-1ZrO_2 was the only material studied whose chemical composition had an excess of oxygen compared to the oxygen content necessary to completely react with the Zr in the material. As oxygen is a potent strengthener of the BCC Nb matrix, it is speculated that interstitial oxygen increased the material's room and elevated temperature strength beyond what is achievable using stoichiometric ZrO_2.

The ZrC nanoparticles processed into the L-PBF consolidated Nb-1ZrC material exhibited a balance of ductility at room/elevated temperature (~20 percent elongation at failure) and moderate strength at elevated temperatures (187 MPa at 1300 °C). The presence of carbon, as measured via LECO combustion analysis to be 576 ppm, may be contributing to both hardening and dynamic strain aging of the material at 1300 °C. As reported in literature (Refs. 6, 20, and 21), carbon acts as an interstitial strengthener within the BCC Nb matrix, restricting dislocation movement. For definitive identification the carbon's role in the Nb-1ZrC material, further investigation via transmission electron microscopy (TEM) is needed to confirm the presence of a (Nb,Zr)C dispersion and the exact strengthening mechanism.

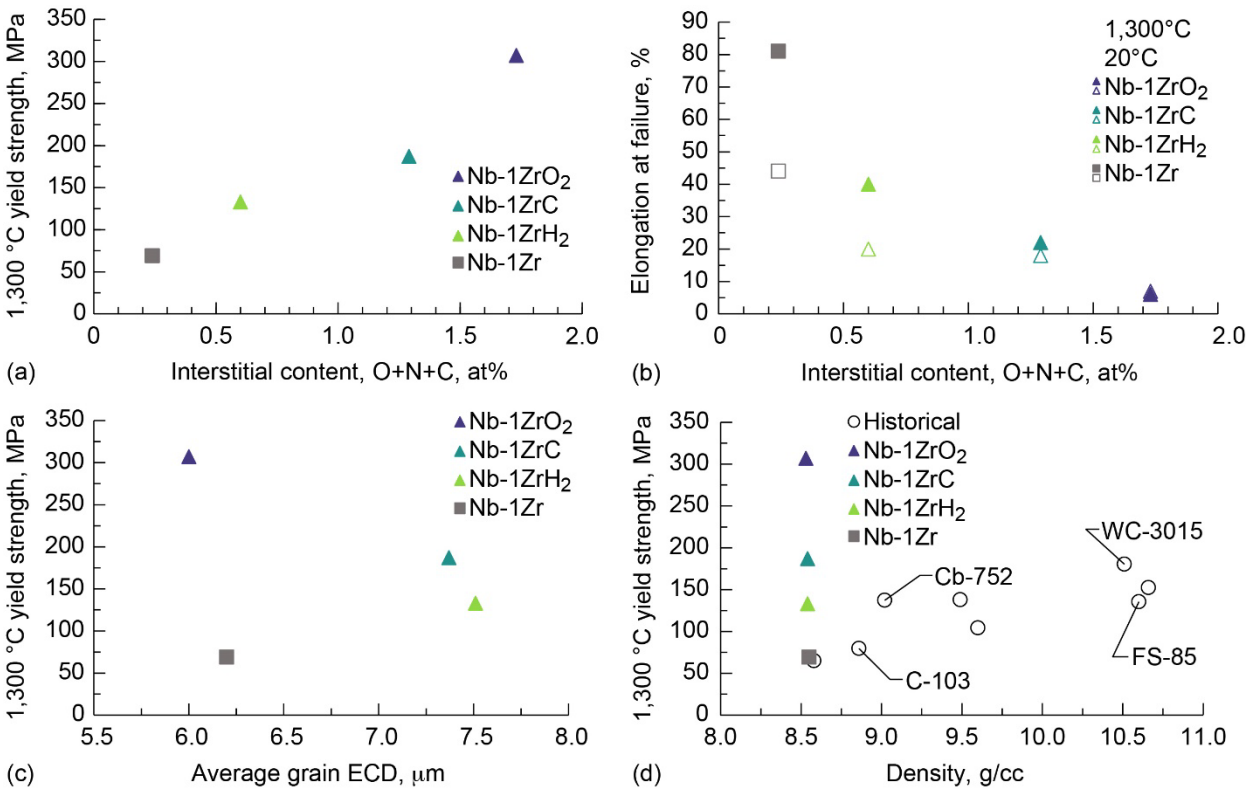

Figure 11.—Analysis of wrought and L-PBF Nb-1Zr material mechanical properties. (a) 1,300 °C yield strength vs. material interstitial content. (b) elongation at failure of 20 and 1,300 °C specimens vs. interstitial content. (c) 1,300 °C yield strength vs. average grain ECD. (d) 1,300 °C yield strength vs. density compared to historical Nb-based alloys.

The Nb-1ZrH_2 material had the lowest elevated temperature yield strength of the L-PBF materials. But it exhibited the closest tensile behavior to the wrought Nb-1Zr counterpart, aligning well with previous observations of improved ductility with increasing Zr content and minimized impurity content (Refs. 2 and 5). The ZrH_2 addition created the greatest ductility at 1300 °C of all the L-PBF consolidated materials with a 40 percent elongation at failure. If the intended application of the material demands exceptional ductility, the ZrH_2 addition would best serve that role. Furthermore, as previously discussed, the Nb-1ZrH_2 material is well suited to tolerate any post processing such as secondary joining methods like laser and election beam welding.

Plots of the 1300 °C yield strength and elongation at failure as a function of interstitial element (oxygen, carbon, and nitrogen) content and average grain equivalent circular diameter (ECD) are shown in Figure 11(a) to (c), respectively. There is a strong linear correlation between the material strength and the combined oxygen, carbon, and nitrogen content (Figure 11(a)). As more oxygen and carbon are added to the composition, an increased volume fraction of ZrO_2 and (Nb,Zr)C are stable in the microstructure which reduce dislocation motion at elevated temperatures. This increase in strength is accompanied by an expected reduction in ductility as seen by the inverse relation between interstitial content and elongation at failure in Figure 11(b). As mentioned, previous study of Nb dispersion strengthening have determined optimal ZrO_2 and (Nb,Zr)C contents of 1 to 2 mol% for maximum hardening at elevated temperatures. The wrought Nb-1Zr, Nb-1ZrO_2, Nb-1ZrC, and Nb-1ZrH_2 materials have theoretical combined ZrO_2 and (Nb,Zr)C contents of 0.25, 1.95, 1.18, and 1.20 mol%, respectively. All L-PBF consolidated materials are within the 1 to 2 mol% range, but the Nb-1ZrO_2 content stands out as the greatest—nearing the maximum

optimal value of 2 mol%. From this understanding, it is expected that the Nb-1ZrC material can be further strengthened with an increased addition of ZrC nanoparticles. No trend was observed between the average grain ECD and elevated temperature strength (Figure 11(c)). However, all specimens studied had similar grain size and texture—which prevents conclusive judgment on the impact of grain size.

5.0 Conclusions

In summary, high purity Nb spherical powder was mixed with 1 wt% additions of ZrO_2, ZrC, and ZrH_2 and consolidated using the laser powder bed fusion process. Short-term elevated temperature tensile testing, density analyses, and detailed electron metallography and fractography provided an understanding of the nano-sized ceramic particle addition's influence on the Nb alloy microstructure and mechanical performance. The aims of the work were to identify the Zr-based ceramic nano-powder addition that produces a balance of elevated temperature strength and room temperature ductility, and evaluate the feasibility of in-situ alloying for fabricating Nb-1Zr alloy components via L-PBF. From the study, the following conclusions can be drawn:

1. In-situ alloying of spherical Nb powder feedstock with Zr-based ceramic nanoparticles successfully produced a Nb-1Zr composition with a Zr content within the ASTM B391 specification (0.8 to 1.2 wt% Zr). A 1 wt% addition of ZrH_2 was sufficient to incorporate 0.83 wt% of Zr in the as-built material. Increased additions of ZrC and ZrO_2 in quantities greater that 1 wt% are also likely to meet the minimum Zr content within the ASTM specification.
2. The ZrH_2 addition achieved the greatest L-PBF relative density compared to the ZrC and ZrO_2 with values of 99.89, 99.75, and 99.5 percent, respectively. Furthermore, the ZrH_2 modified material exhibited identical (90°) hammer-bend test performance to wrought Nb-1Zr; proving L-PBF consolidated material can provide adequate room temperature ductility.
3. Both the ZrC and ZrH_2 modified Nb feedstocks showed ductile fracture features, especially at 1300 °C. The carbide addition increased short-term elevated temperature strength compared to the hydride with yield strengths at 1300 °C of 187 and 133 MPa, respectively. However, this increase in elevated temperature strength was accompanied by a reduction in ductility (22 percent (ZrC) versus 40 percent (ZrH_2) elongation at failure).
4. The ZrO_2 addition offered the greatest elevated temperature strength. But the material suffered from brittle behavior with a room temperature ductility of 6 percent elongation at failure. The Nb1-ZrO_2 was the only L-PBF consolidated material that did not form grain boundary precipitates during the 30-min 1300 °C exposure indicating a more thermally stable microstructure.

References

1. R.H. Titran, "Long-Time Creep Behavior of Nb-1Zr Alloy Containing Carbon," in TMS-AIME Fall Meeting, Orlando, 1986.
2. E.S. Bartlett and J.A. Houck, "Physical and Mechanical Properties of Columbium and Columbium-Base Alloys," Defense Metals Information Center, Columbus, 1960.
3. A.G. Imgram and H.R. Ogden, "The Effect of Fabrication History and Microstructure on the Mechanical Properties of Refractory Metals and Alloys," Defense Metals Information Center, Columbus, 1963.
4. B.K. Grigorovich and E.N. Sheftel, Dispersion Hardening of Refractory Metals, Moscow: Nauka Publishing House, 1980.

5. D.O. Hobson, “Effect of Alloying Elements on the Strength, Stability, and Corrosion and Oxidation Resistance of Columbium,” Oak Ridge National Laboratory, Oak Ridge, 1962.
6. E.M. Savitskii and G.S. Burkhanov, Physical Metallurgy of Refractory Metals and Alloys, New York: Consultants Bureau, 1970.
7. V.G. Grigorovich and E.N. Sheftel, “Physiochemical Fundamentals of the Development of Heat-resistant Niobium Alloys,” Metallovedenie i Termicheskaya Obrabotka Metallov, vol. 7, pp. 23–29, 1982.
8. B. Vishwanadh, K.V. Mani Krishna, A. Upadhyay, R. Banerjee, A. Arya, R. Tewari, H.L. Fraser and G.K. Dey, “Formation mechanism of the Nb2C phase in the Nb-1Zr-0.1C (wt%) alloy and interrelation between y, B, and a-Nb2C carbide phases,” Acta Materialia, vol. 108, pp. 186–196, 2016.
9. B. Vishwanadh, A. Arya, R. Tewari, and G.K. Dey, “Formation mechanism of stable NbC carbide phase in Nb-1Zr-0.1C (wt%) alloy,” Acta Materialia, vol. 144, pp. 470–483, 2018.
10. T.L. Grobstein and R.H. Titran, “Characterization of Precipitates in a Niobium-Zriconium-Carbon Alloy,” in TMS-AIME Fall Meeting, Orlando, 1986.
11. P. Hu, T. Chang, Z. Yu, F. Yang, B. Hu, Y. Zhou, K. Wang, W. Cao, D. Liu, and A.A. Volinsky, “Synthesis of hypoxia-high density TZM alloy based on,” Journal of Alloys and Compounds, vol. 698, pp. 994–1001, 2017.
12. P.R. Gradl, O.R. Mireles, C.S. Protz, and C.P. Garcia, Metal Additive Manufacturing for Propulsion Applications, Reston: American Institute of Aeronautics and Astronautics, 2022.
13. ASTM International, B391-18 Standard Specification for Niobium and Niobium Alloy Ingots, West Conshohocken: ASTM International, 2018.
14. F.F. Schmidt and H.R. Ogden, “The Engineering Properties of Columbium and Columbium Alloys,” Defense Metals Information Center, Columbus, 1963.
15. E. Brizes and J.L. Milner, “Electron Beam Welding of Additively Manufactured,” National Aeronautics and Space Administration, Cleveland, 2023.
16. L.J. Pionke and J.W. Davis, “Technical Assessment of Niobium Alloys Data Base for Fusion Reactor Applications,” The U.S. Department of Energy, 1979.
17. K.J. Leonard, J.T. Busby and S.J. Zinkle, “Influence of thermal and radiation effects on microstructural and mechanical,” Journal of Nuclear Materials, vol. 414, pp. 286–302, 2010.
18. C. English, “The Physical, Mechanical, and Irradiation Behavior of Niobium,” AERE Harwell, Oxfordshire, 1981.
19. R.C. Svedberg and R.L. Ammon, “Oxidation Resistant Niobium Alloy,” United States of America Patent 4,836,849, 6 June 1989.
20. D.L. Anton, D.B. Snow, L.H. Favrow, and A.F. Giamei, “Dispersion Strengthening of High Temperature Niobium Alloys,” Air Force Office of Scientific Research, Washington D.C., 1989.
21. A.N. Behera, A. Chaudhuri, R. Kapoor, J.K. Chakravartty, and S. Suwas, “High temperature deformation behavior of Nb–1 wt.%Zr alloy,” Materials and Design, vol. 92, pp. 750–759, 2015.